The interaction of intense, ultra-short microwave beams with the plasma generated by gas ionization

G. Shafir,[1] Y. Cao,[1] Y. Bliokh,[1] J. G. Leopold,[1] D. Levko,[2] V. Rostov,[3] R. Gad,[1] A. Fisher,[1] V. Bernshtam,[4] and Ya. E. Krasik[1]
[1]*Physics Department, Technion, Haifa 32000, Israel*
[2]*Department of Aerospace Engineering and Engineering Mechanics, University of Texas, Austin, Texas 78712, USA*
[3]*Institute of High Current Electronics, RAS, Tomsk 634055, Russia*
[4]*Faculty of Physics, Weizmann Institute of Science, Rehovot 36100, Israel*

(Received 27 January 2018; accepted 6 March 2018; published online 22 March 2018)

Results of the non-linear interaction of an extremely short (0.6 ns) high power (~500 MW) X-band focused microwave beam with the plasma generated by gas ionization are presented. Within certain gas pressure ranges, specific to the gas type, the plasma density is considerably lower around the microwave beam axis than at its periphery, thus forming guiding channel through which the beam self-focuses. Outside these pressure ranges, either diffuse or streamer-like plasma is observed. We also observe high energy electrons (~15 keV), accelerated by the very high-power microwaves. A simplified analytical model of this complicated dynamical system and particle-in-cell numerical simulations confirm the experimental results. *Published by AIP Publishing.*
https://doi.org/10.1063/1.5023715

I. INTRODUCTION

The non-linear interaction of pulsed high-power microwaves with gas and plasma has been studied extensively over the years. These studies are important to subjects such as the generation and propagation of microwave beams,[1–3] ponderomotive force research including wakefield generation and charged particle acceleration,[4–8] atmospheric environmental research,[9] high power microwave compressors,[10,11] and plasma heating and various instabilities.[12,13]

For high power densities ($\geq 10^7$ W/cm^2) of the microwave beam propagating in gas, intriguing non-linear phenomena occur when the energy, $\tilde{\varepsilon} = e^2E_0^2/2m(\omega^2+\nu^2)$, which the plasma electrons gain in the microwave electric field, exceeds the ionization energy, ε_i. Here e is the electron charge, m is the electron mass, E_0 is the amplitude, ω is the angular frequency of the microwave electric field, and ν is the electron-neutral momentum transfer collision frequency. It is important to note that the plasma generation by sub-ns and high electric field (>100 kV/cm) microwave beams due to ionization of gas requires extremely high ionization frequency.[14]

In earlier experimental studies, the interaction of high-power, $E_0 \leq 100$ kV/cm, microwave beams with different gases was studied with pulses in the tens of nanoseconds (>30 ns)[9,15–17] and microsecond (>10^{-5} s)[18–21] timescales. For short pulses, at gas pressures $P \leq 15$ Pa, the gas discharge appears diffused in space. For higher pressure discrete streamer-like plasma structures appear, each representing an avalanche from an initial seed electron. The latter phenomenon is related to high electron impact ionization rates during the short microwave pulse.[18] Other experiments[22,23] reported the build-up of high plasma positive potentials (up to 15 kV) and high-energy electrons (up to 25 keV), in a plasma produced by the interaction of a focused microwave beam (E_0 ≈100 kV/cm, 50 ns pulse length, $f = 10$ GHz) with a dielectric target. The latter leads to charged plasma particle separation and the formation of quasi-stationary electric fields leading to acceleration of part of the plasma electrons to keV energies. Yalandin *et al.*[24,25] reported experimental results on breakdown electric field thresholds in air for nanosecond and sub-nanosecond high-power (up to 500 MW) microwave beams in the Ka-band. However, the plasma produced by such beams has not been characterized yet.

Interaction of strong microwave fields with gas resulting in over-dense plasma formation occurs in an interference plasma switch and is crucial for the efficient operation of high power microwave compressors. To release the microwave energy stored in the resonant cavity of a compressor with the highest efficiency, the over-dense plasma layer is required to form in a sub-nanosecond timescale. Beilin *et al.*[10] and Shlapakovski *et al.*[11] showed that the over-dense streamer-like plasma is generated inside such an interference switch within a typical time scale of ~1 ns, while the plasma density increases up to ~10^{16} cm^{-3} for a microwave ($f \approx 3$ GHz) field of ~50 kV/cm.

Other phenomena, associated with nanosecond and sub-nanosecond high-power microwave beam interaction with plasma, are frequency upshifting and ionization self-channeling. Frequency upshifting of the microwave beam occurs either when one obtains an almost simultaneous increase in the plasma density in a space exceeding the electromagnetic wavelength,[26] or when the plasma is rapidly expanding towards the microwave beam.[27] The theory of microwave frequency upshift and plasma formation by gas ionization was developed by Gil'denburg *et al.*,[28] and these phenomena were experimentally observed by Kuo[29] using fast plasma formation due to gas ionization by two intersecting microwave beams.

Ionization-induced self-channeling of microwave beams was theoretically predicted by Bogomolov *et al.*[30] for pulsed, high-power microwave beams with Gaussian radial distribution. It was shown that when the oscillatory energy of the plasma electrons exceeds considerably the ionization energy

of neutral atoms, the impact ionization rate at the beam periphery becomes larger than that at the beam axis. This is due to the significantly larger electron energy and, respectively, smaller ionization cross-section at the center of the beam than at its periphery. Thus, for very high-power microwave beams, it is possible to obtain over-dense plasma at its periphery and under-dense plasma in its central region. This effect was not observed experimentally so far.

In this paper, we report the results of experimental and numerical investigation of the interaction between extremely short pulses [$\tau = 0.6$ ns at full width at half maximum, (FWHM)], of a high-power microwave beam, $f = 9.6$ GHz, $E_0 \approx 150$ kV/cm, with air and He at various pressures. The microwave beam's propagation, as well as the generated plasma parameters, was investigated using time- and space-resolved electrical, optical, and spectroscopic diagnostics. By focusing such high-power microwave beams into a neutral gas using a dielectric lens, we produced a cylindrical plasma with minimal density at its center and observed the consequences of the microwave beam's self-channeling in this "hollow" plasma channel. Such results have not been observed before. These experimental results were confirmed by an analytical model, by 1-D particle-in-cell (PIC) combined with Monte Carlo collisions simulations[31] on the focal plane and by 2D large scale plasma (Lsp) hybrid simulations[32,33] of the microwave beam's reactive propagation in the gas. In addition, sub-nanosecond formation of either diffuse or streamer-like (depending on gas pressure) plasma channels was observed as well as high energy (>15 keV) electrons in plasma.

II. EXPERIMENTAL SETUP AND DIAGNOSTICS

The experimental setup is shown in Fig. 1. The microwave generator is a super-radiance backward wave oscillator (BWO),[34] driven by an all solid-state generator,[35] which produces at its output on a 200 Ω matched load a 350 kV, ~0.5 ns rise time, ~6 ns (FWHM) long pulse.[4] This voltage pulse was applied to a sharp edged circular graphite cathode of a magnetically insulated foil-less diode, resulting in the generation of a hollow ~280 keV electron beam. A guiding magnetic field of 2.5 T and half-period of 2 ms was produced by a solenoid powered by a capacitor (4 mF, 1.6 kV) discharge.

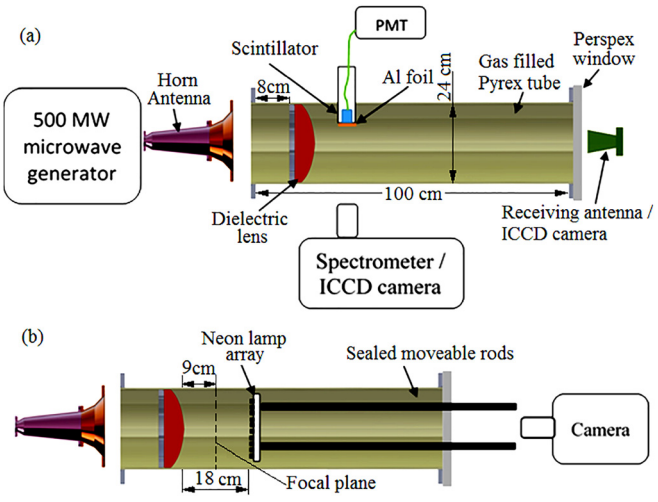

FIG. 1. Schematic drawing of the experimental setup, including the microwave generator, antenna, dielectric lens, and the gas filled Pyrex tube. The various diagnostic tools and their specific location and use are detailed in the text.

The microwave radiation, with peak power up to 550 MW, frequency $f = 9.6$ GHz, and pulse duration $\tau \approx 0.6$ ns FWHM, is generated in the BWO with a diameter of 32 mm.[4] A mode converter connected to the BWO output transforms the TM_{01} mode (operating mode of the BWO) into a TE_{11} mode. The latter radiates in the form of a linearly polarized Gaussian beam through a specially designed cylindrical horn antenna. The microwave beam has a width of ~2.7 cm FWHM, ~9 cm upstream from the antenna output aperture. This beam is then focused using a specially designed dielectric (Ultem) lens into a 24 cm diameter, 100 cm long Pyrex tube. The lens has a cylindrically hyperbolic profile with a focal plane located 9 cm from the tip of the lens. The tube was either evacuated of air to a pressure of 15 mPa or filled with He gas or air within the pressure range 100 Pa to 10^5 Pa.

The waveforms of the voltage and the total current of the diode were monitored using a capacitive voltage divider and a self-integrated Rogowski coil, respectively. The radial distribution and waveform of the transmitted radiation were measured at the output of the Pyrex tube by a standard WR90, 10 dB gain receiving antenna and recorded by a 12 GHz digitizing oscilloscope (Agilent DSO81024B). The transverse power distribution of the microwave radiation at various longitudinal positions inside the Pyrex tube was observed by an array of 400 miniature Ne lamps, 4 mm diameter each. All microwave measurements were performed inside a specially built anechoic room (2 m × 1.2 m × 1.8 m) covered by microwave absorbing material (17 dB at 10 GHz).

The plasma light emission for various gases and pressures was studied using a photomultiplier tube, PMT (Hamamatsu H10721), placed inside a screen box with lenses adjusted to collimate the light emitted by the plasma from the focal region (see Fig. 1). Side view images (with respect to the microwave beam axis) of the plasma light emission were obtained using three cameras: a digital camera (Nikon D300s) obtained time integrated images with a 72 cm long field of view; a 4QuikE single frame intensified camera (Stanford Computer Optics) took images with frame duration of 1.2 ns and with a 30 cm long field of view; and an XXRapidFrame four-frame intensified camera (Stanford Computer Optics) took four images each with a frame duration of 0.5 ns and a time delay as short as 0.7 ns between frames. For the latter, the field of view was 10 cm long. Front view images of the plasma light emission were obtained by the 4QuikE with a frame duration of 1.2 ns, focused to the microwave beam's focal plane.

To estimate the energy of the plasma electrons, an Ej-228 scintillator (0.5 ns rise time, 1.5 ns decay time) was used, with thin (10–20 μm) Al foils placed at its front surface. The scintillator was placed inside the Pyrex tube at a radius of 5 or 8 cm from the axis along the focal plane. The scintillator was coupled to an optical fiber connected to a PMT (Hamamatsu R7400U), placed in a screen box.

The parameters of the plasma, generated by microwave ionization of He, were studied using optical emission spectroscopy. To measure the line intensity of the He spectral lines, an

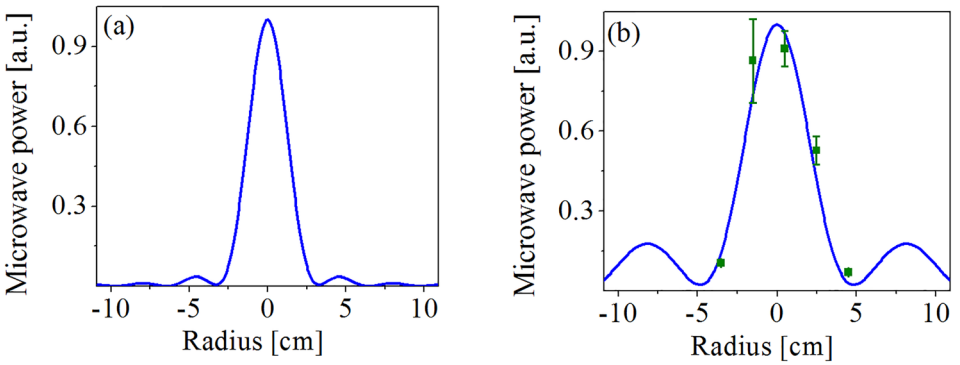

FIG. 2. MAGIC simulated radial distribution of the microwave power in vacuum (a) 9 cm from the lens tip (the focal plane) and (b) 120 cm from the lens tip (blue line) compared to the measured full power (green squares).

optical setup consisting of mirrors, lenses, and an imaging spectrometer (Chromex 250i) with the 4QuikE camera at its output was used. The absolute calibration of this optical setup was carried out using a calibrated Tungsten lamp (Oriel model 63355). These measurements allowed us to determine the population of the energy levels of the excited atoms and ions and, consequently, to calculate the density of atoms and ions using atomic data. In the experiments, we measured the population of the 1s3d(^{3}D), 1s3d (^{1}D), 1s3p(^{3}P), 1s4s (^{1}D), and 1s4d (^{1}D) states of He I, as well as the population of the He II, $n = 4$ energy level. The line intensities were compared with the results of time-dependent collisional radiative modeling[36] of the corresponding levels' population. In this model, we used the time-dependent electron energy distribution functions obtained from our one-dimensional (1D) PIC simulations.

III. EXPERIMENTAL RESULTS

For full microwave power of the beam generated by the BWO, the radial distribution of the beam intensity near the focal region was not measured because of electrical breakdown inside the receiving antenna. Instead, using a network analyzer a low power 9.6 GHz TE11 microwave was fed into the horn antenna and the axial distribution of the microwave power inside the Pyrex tube was measured by moving the receiving antenna along the tube axis. Results of these measurements showed good agreement with MAGIC[37] 3-D electromagnetic simulations carried out for 9.6 GHz TE11 microwaves focused by the Ultem lens and propagating inside the Pyrex tube. This allows one to confirm that at the focal plane, the microwave beam has a Gaussian profile, $P(r,t) \propto \exp(-t^2/\tau_{\text{beam}}^2)\exp(-r^2/r_{\text{beam}}^2)$, where $\tau_{beam} \approx 0.37$ ns (0.6 ns at FWHM) and $r_{beam} \approx 1.6$ cm [Fig. 2(a)] and that the electric field maximum is ~150 kV/cm for 500 MW microwave input power. The Rayleigh length of the beam is ~5.4 cm.

In experiments with microwave beam generated by BWO, at the plane of the receiving antenna, placed 120 cm from the focal plane, the Gaussian microwave beam's width is $r_{beam} \approx 3$ cm [Fig. 2(b)] and the power density on axis was 500 ± 50 kW/cm^2, which corresponds to an electric field amplitude of $E = 20 \pm 0.1$ kV/cm. The radial profile of the beam power was found in good agreement with the results of the MAGIC simulated radial distribution of the microwave power at that distance [see Fig. 2(b)]. The temporal profile of the microwave pulse propagating in vacuum remained unchanged.

When the Pyrex tube was filled by either He or air, the temporal profile and the transmitted power changed because of plasma formation due to microwave beam induced gas ionization. The dependence of the peak microwave power normalized to its maximum value in vacuum measured at $z = 120$ cm as a function of the air and He gas pressure is shown in Fig. 3. One can see that for the pressure range of $10^3 < p < 10^4$ Pa of air and $6 \times 10^3 < p < 2 \times 10^4$ Pa of He, only ~30% and ~50% of the microwave beam power reaches the output of the Pyrex tube, respectively. Outside these pressure ranges, one can assume that insufficient plasma density is formed by the microwave beam during ~0.5 ns. At the same time, compared to vacuum, no significant change in the radial distribution of the beam power, measured by the receiving antenna at the output of the Pyrex, was detected.

Typical temporal dependence of the microwave power, measured by the receiving antenna on axis, at $z = 120$ cm in vacuum is compared with measurements at various pressures in air [Fig. 4(a)] and He [Fig. 4(b)]. In vacuum, the temporal

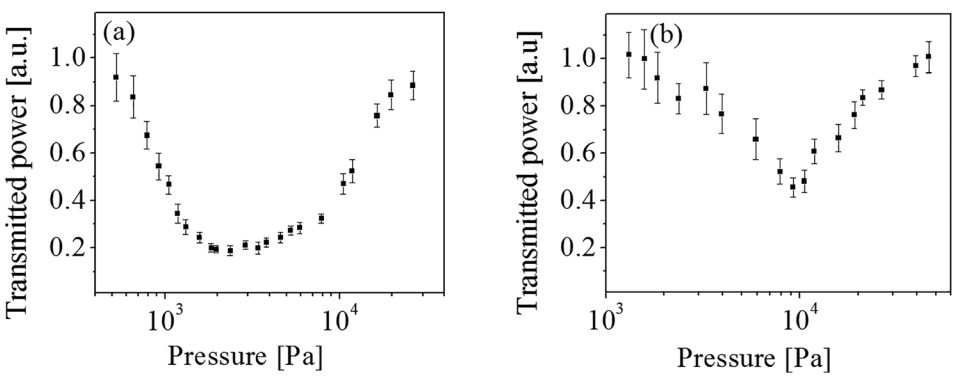

FIG. 3. Transmitted microwave power, measured at the receiving antenna, versus the gas pressure, for air (a) and He (b).

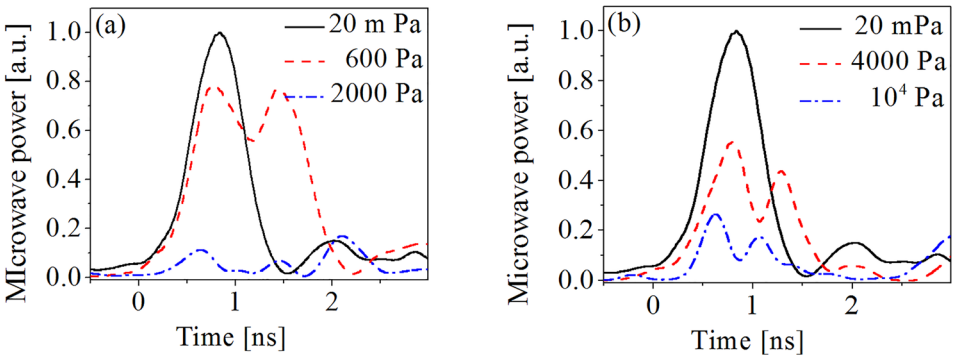

FIG. 4. Typical temporal dependence of power of the transmitted signal, measured at the receiver antenna, at different gas pressures for (a) air and (b) He. The amplitude of the power is normalized to that obtained in vacuum.

profile of the measured power is Gaussian, identical to the profile of the microwave pulse generated by the BWO. In the pressure regions, $5 \times 10^2 < p < 10^3$ Pa and $3 \times 10^3 < p < 6 \times 10^3$ Pa for air and He, respectively, the waveform of the microwave power changed significantly showing two distinct peaks, separated by 0.5–0.8 ns. This temporal form of the microwave power relates to the dynamics of the plasma formation and will be discussed in Sec. IV. For the pressure ranges, $10^3 < p < 10^4$ Pa and $6 \times 10^3 < p < 2 \times 10^4$ Pa for air and He, respectively, the measured power waveforms were irregular and it was difficult to distinguish two peaks. One can assume that within these pressure ranges, the plasma density was close to or higher than the critical density blocking most of the power and leaving only some reflected and scattered microwaves to reach the receiving antenna. At higher pressures, $p > 10^4$ Pa and $p > 2 \times 10^4$ Pa for air and He, respectively, the temporal profile of the microwave beam power was similar to that obtained in vacuum. The latter can be related either to plasma generation in a volume with a much smaller cross-sectional area than the beam cross section, or that there is insignificant ionization resulting in only low-density plasma generation. These issues will be addressed in Sec. IV.

The transverse power distribution of the microwave beam at a distance of 10 cm downstream from the focal plane was observed by the Ne lamps array. Typical images of these patterns are presented in Fig. 5 for air and He at various pressures. For vacuum and atmospheric pressure air, the pattern diameter was ~9 cm [Figs. 5(a) and 5(d)], which agrees with the expansion of the Gaussian beam at this position in vacuum obtained by MAGIC simulations. When the Pyrex tube was filled with gas, within the pressure range $5 \times 10^2 < p < 10^3$ Pa for air or $3 \times 10^3 < p < 6 \times 10^3$ Pa for He, the pattern diameter decreased to ~4–5 cm [Figs. 5(b) and 5(e)], suggesting that only the central part of the beam propagated. For higher gas pressure ranges, $10^3 < p < 10^4$ Pa and $6 \times 10^3 < p < 2 \times 10^4$ Pa for air and He, respectively, light emitted by the Ne lamps was negligible, indicating that the beam was significantly attenuated until it reached the array. The latter can be associated with a dense plasma formation near the focal plane.

Finally, for the highest pressure ranges considered, $10^4 < p < 3 \times 10^4$ Pa and $2 \times 10^4 < p < 4 \times 10^4$ Pa for air and He, respectively, a hollow structure of the microwave beam pattern was observed [Figs. 5(c) and 5(f)]. This can be qualitatively explained by over-dense plasma formation at the focal location around the beam axis, allowing microwave transmission only at the beam periphery. Within this pressure range, the diameter of the hollow pattern decreases with increasing gas pressure, until almost the entire Ne lamps array lights up.

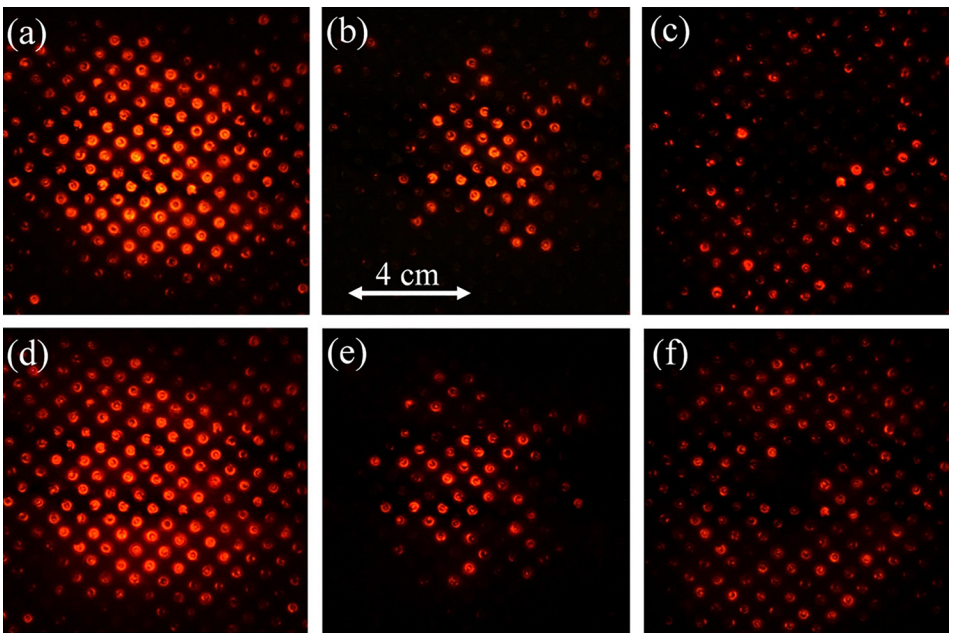

FIG. 5. Time integrated patterns of the microwave beam power distribution, measured by the array of Ne lamps at the distance of 10 cm from the focal plane: (a) 20 mPa; (b) He: 4.5×10^3 Pa; (c) He: 3×10^4 Pa; (d) air: 10^5 Pa; (e) air: 7×10^2 Pa; (f) air: 10^4 Pa.

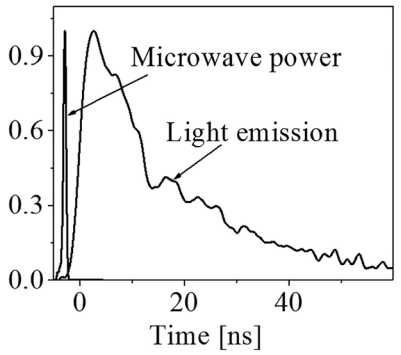

FIG. 6. A typical plasma light emission waveform obtained by the PMT viewing the focal region for air at $p = 10^3$ Pa relative to the almost, on this timescale, singular waveform of the input microwave power. The time $t = 0$ is defined as the beginning of light emission from the plasma.

When the array of neon lamps was placed further away, 15 cm, or closer, 5 cm, relative to the focal plane, almost the same results were obtained as at 10 cm.

A typical temporal evolution of the plasma light emission from the focal location, obtained by the collimated PMT, is shown in Fig. 6 together with the microwave input power, for air at $p = 10^3$ Pa. Here, $t = 0$ is defined as the start time of the light emission from the focal plane. One can see that the beginning of the light emission is delayed relative to the peak power of the microwave pulse by ~3 ns. The latter can be related to the finite lifetimes of the electronically excited plasma atoms and ions. The measured duration of the light emission decreased with the increase in air pressure from ~15 ns FWHM at $p = 5 \times 10^2$ Pa down to ~5 ns at $p = 3 \times 10^4$ Pa. This is related to increase in the rate of plasma recombination at higher pressures and faster electron cooling. For He, similar results were obtained; namely, the duration of the light emission was ~25 ns at $p = 10^3$ Pa and ~7 ns at $p = 6 \times 10^4$ Pa. At higher or lower gas pressures than the above pressure ranges, the intensity of the plasma light emission decreases drastically to almost non-detectable level.

In Figs. 7 and 8, fast framing images of the light emission from the plasma, obtained by the XXRapidFrame camera, are shown, where the four frames in a row of pictures were obtained during the same generator shot. The exposure time was 0.5 ns and 1.5 ns, and the time between frames was 0.7 and 2 ns for air and He, respectively. The light emission patterns of the generated plasma are similar for air and He but for different ranges of pressures. Diffused plasma patterns were obtained at $p < 2 \times 10^3$ Pa ($p = 10^3$ Pa, first row in Fig. 7) and $p < 5 \times 10^3$ Pa ($p = 2 \times 10^3$ Pa, first row in Fig. 8) for air and He, respectively. This diffused light emission starts from discrete and randomly distributed spots which quickly expand and overlap (especially for He), during the time the microwave beam's crossing. As the gas pressure

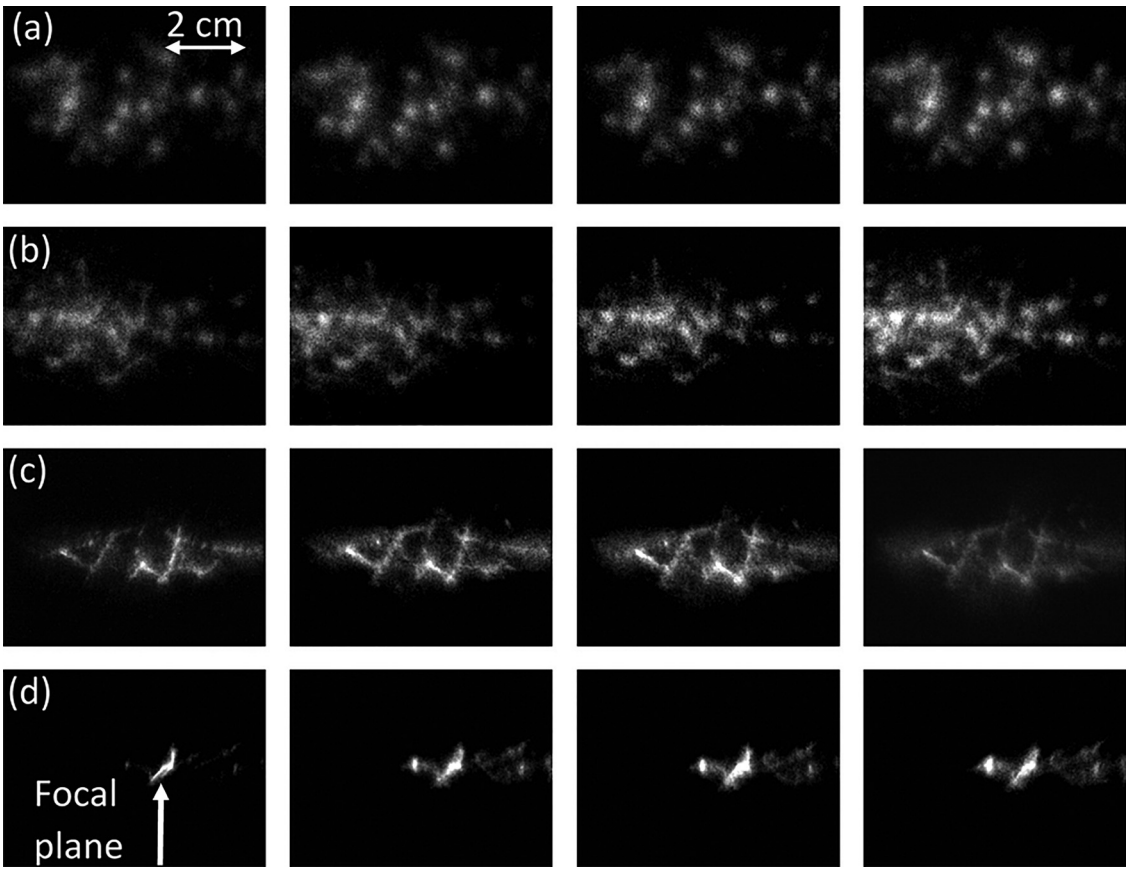

FIG. 7. Fast framing images of the plasma light emission from the focal location, obtained by the XXRapidFrame camera, for air. Each row represents four images taken during the same generator shot, with the frame duration of 0.5 ns, and delay between frames of 0.7 ns (from left to right). First image was obtained at $t = 0$ (the beginning of the light emission). (a) $p = 10^3$ Pa; (b) $p = 2 \times 10^3$ Pa; (c) $p = 1.5 \times 10^4$ Pa; and (d) $p = 3 \times 10^4$ Pa. The microwave beam propagates from left to right.

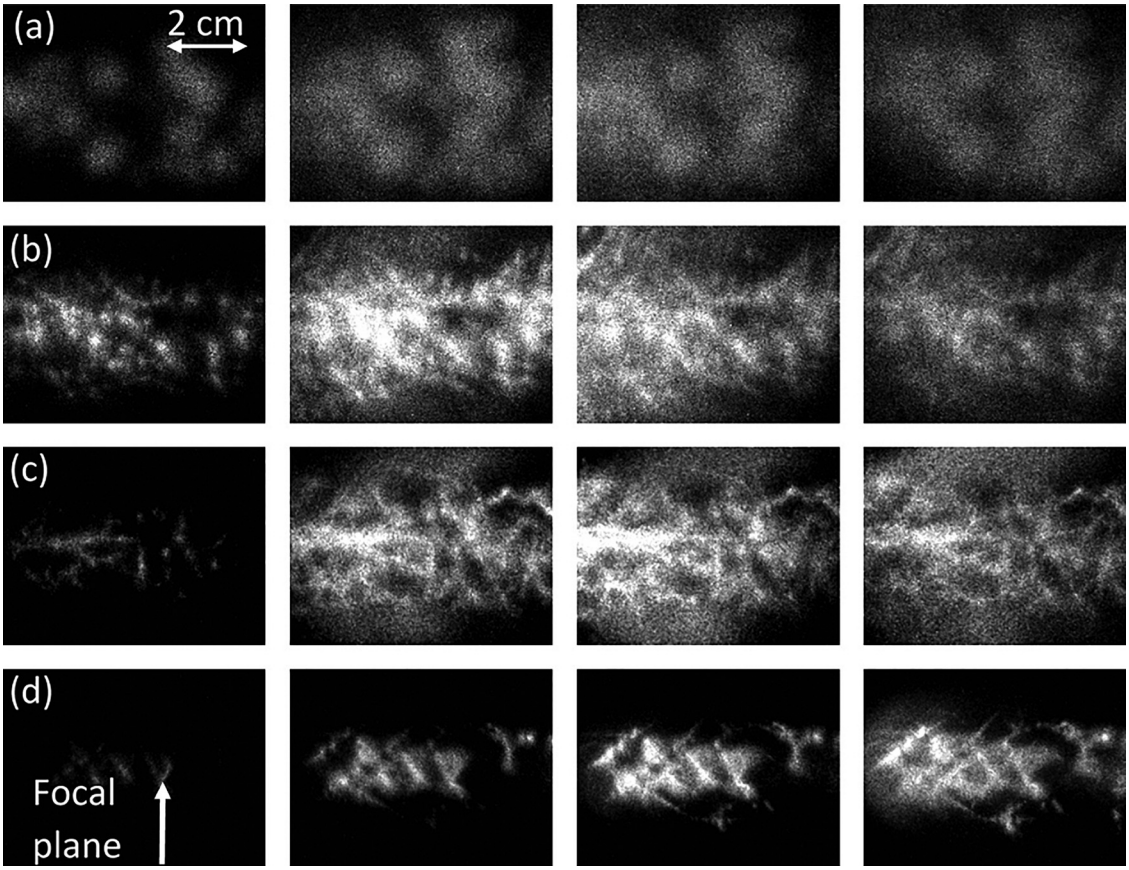

FIG. 8. Same as Fig. 7 for He, with the frame duration of 1.5 ns, and delay between frames of 2 ns, at (a) $p = 2 \times 10^3$ Pa; (b) $p = 1.5 \times 10^4$ Pa; (c) $p = 3 \times 10^4$ Pa; and (d) $p = 5 \times 10^4$ Pa.

is increased $2 \times 10^3 < p < 4 \times 10^3$ Pa and $p > 2 \times 10^4$ Pa for air and He, respectively, the radius of the light emitted area reduces and streamer develops.

In Fig. 9, typical fast framing images of the plasma light emission from a wider field of view (17 cm), obtained by the 4QuikE camera, are shown. For these conditions, only a single image of the plasma was obtained for each generator shot. The light emission is shown for air at $p = 10^3$ Pa, from $t = 0$ to 6 ns with 1 ns between frames.

One can see that during the first ns, the light is visible only in the volume around the focal plane. Then, light develops behind and in front of the increasingly intense light from the focus. Since the microwave beam pulse length and propagation time are <1 ns, by the time most of these frames were taken, the microwave pulse has already left this region. The distribution of the plasma light emission between the lens and the focal plane follows the convergence of the microwave beam toward the focal plane with maximal electric field at that location, as seen in MAGIC simulations in vacuum [Fig. 9(g)]. Similar light emission patterns were obtained for almost all other experimental conditions except $p > 10^4$ Pa in air and $p > 4 \times 10^4$ Pa in He. At these pressures, the plasma emitted intense light only close to the focal region.

Finally, wide (72 cm) field of view patterns of the plasma light emission, taken by the Nikon D300S digital camera, operated with open shutter obtaining time-integrated light emission of the plasma generated by the microwave beam propagation in air and He, for different pressures are shown in Fig. 10.

In Figs. 10(a)–10(f), for gas pressures within the range, $6 \times 10^2 < p < 3 \times 10^3$ Pa in air and $3 \times 10^3 < p < 1.5 \times 10^4$ Pa in He, a plasma channel longer than the Rayleigh length is seen. In particular, for 10^3 Pa He the plasma channel is ~40 cm long and ~4 cm in diameter, ~7 times longer than the Rayleigh length. This is too long to be the results of simple microwave beam propagation as in vacuum [see Fig. 10(g)]. This observation will be discussed in Sec. IV.

Front views of the plasma light emission at the beginning of the light emission are shown in Fig. 11 for both air and He at various pressures. These images were obtained by the 4QuikE camera focused to the focal plane and operating with a frame duration of 1.2 ns.

One can see within a ~4 cm diameter area, approximately uniform distribution of the plasma light emission for $p = 1.5 \times 10^4$ Pa in air [Fig. 11(b)] and for $p = 3 \times 10^4$ Pa in He [Fig. 11(d)]. However, for $p = 10^3$ Pa in air and $p = 4.5 \times 10^3$ Pa in He, a hollow central region is seen [see Figs. 11(a) and 11(c), respectively]. A sequence of frames in time show that this hollow structure light intensity appears during ≤1 ns and later it transforms to uniform distribution. This indicates that a hollow cylindrical plasma with reduced density around the axis develops at focus during the time interval when the microwave beam pulse crosses this plane. These observations agree qualitatively with the data obtained by the array of Ne lamps for the same plasma range, showing a light pattern only close to the axis which indicates that the microwave beam's periphery was cut off by the plasma [see Figs. 5(b) and 5(e)].

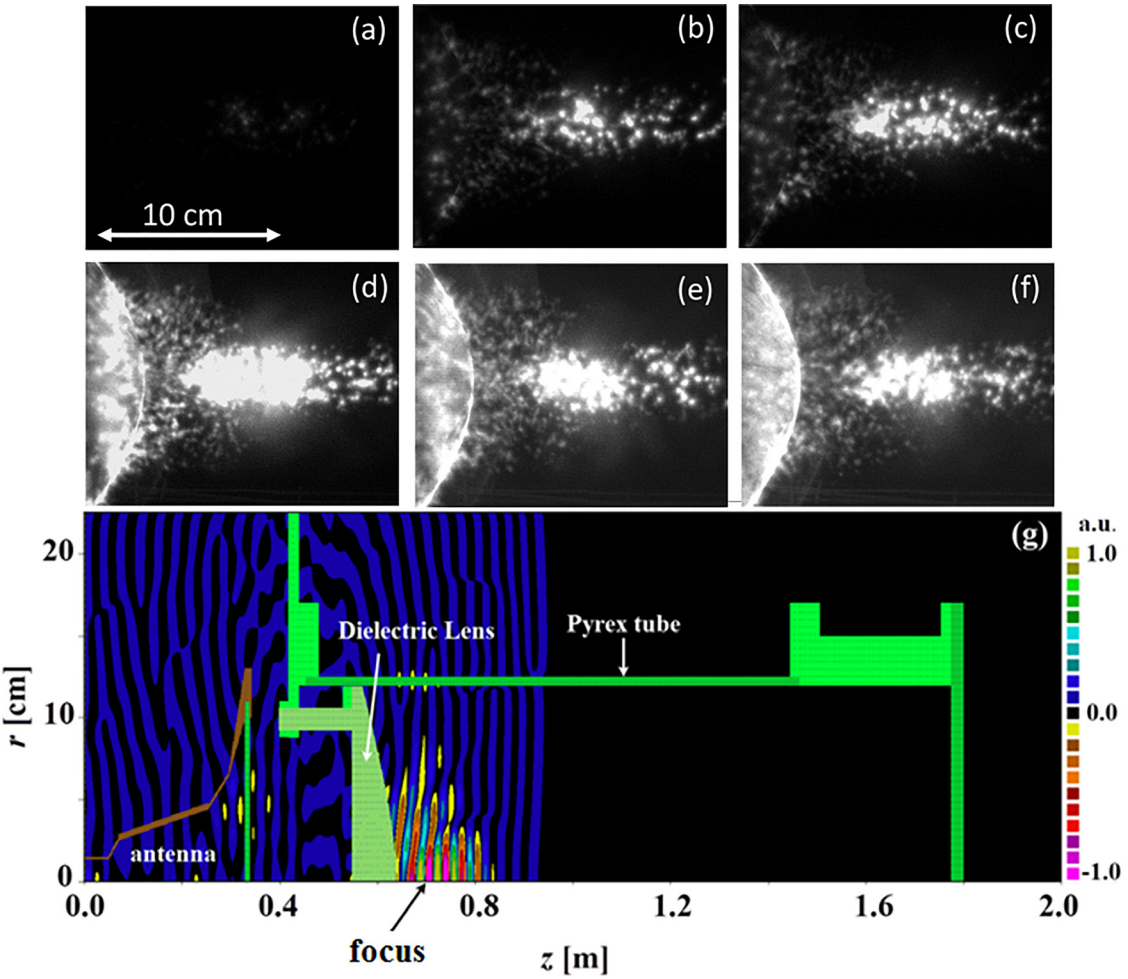

FIG. 9. Fast framing images of the plasma light emission taken from the lens downstream including the focus, by the 4QuikE camera, for air at $p = 10^3$ Pa. Each frame is 1.2 ns long with 1 ns between frames. The first frame (a) was obtained at $t = 0$ (beginning of the light emission). Each frame was obtained for different generator shots. For comparison, the PIC simulated contours of the radial component of the electric field pulse in vacuum at the time when it crosses the focal plane is seen in (g). (The green surfaces represent the dielectric walls of the experimental system. The antenna delivering the microwave pulse from the exit of the mode-converter towards the plasma chamber is seen at the upstream edge of the simulation region.)

We estimated the plasma electron energy by measuring the luminescence generated by electrons interacting with the plastic scintillators covered by thin Al foils which block all other light. The scintillator, coupled to an optical fiber, was placed at distances of $r = 4.5$ cm from the axis of the Pyrex tube, on the focal plane. In Fig. 12, typical luminescence signals are shown for 10 μm and 20 μm thick Al foils. For 30 μm thick Al foil, no luminescence was observed.

Stopping range data for electrons in Al[38] suggests the presence of plasma electrons of energies $\geq$15 keV. The presence of such high energy electrons can only be because of the high accelerating electric fields within the focal region. Results similar to those seen in Fig. 12 were obtained for air within the pressure range $5 \times 10^2 < P < 6 \times 10^3$ Pa. Outside this range, for both lower and higher pressures, the PMT signal was below the noise level, indicating that energetic electrons are confined close to the axis.

The plasma density was determined using the absolute calibrated spectroscopy system. The sensitivity of the optical setup allowed measurement of plasma density $\geq 2 \times 10^{13}$ cm^{-3}. In these experiments, the 4QuikE camera frame duration was varied in the range of 1.2–10 ns, determined by the conditions necessary to obtain reliable spectral line intensities. Typical spectral line intensities of He I excited atoms 471.31 nm (1s2p-1s4s) and He II ions 468.58 nm (3d-4f) are shown in Fig. 13.

Strong light emission from He II ions, obtained for frame durations of 2 ns close to the beginning of light emission, strongly supports the existence of energetic electrons. For all cases, the FWHM of the measured spectral lines was almost equal to the instrumental broadening which means that Doppler and Stark broadening were negligibly small. Therefore, the population of the excited levels was derived directly from the line intensities. The measured level populations were compared with the results of the time-dependent collisional radiative modeling of the corresponding level populations.[36] This modeling was carried out with the time-dependent electron energy distribution functions obtained from PIC simulation (see Sec. IV). The population of the energy levels, obtained for excited He I atoms and He II ions at $P = 4.5 \times 10^3$ Pa, is presented in Table I.

The plasma electron density corresponding to these populations was found to be in the range $2 \times 10^{14} < n_e < 8 \times 10^{14}$ cm^{-3}. This density agrees well with the value of the density obtained in PIC simulations (see Sec. IV).

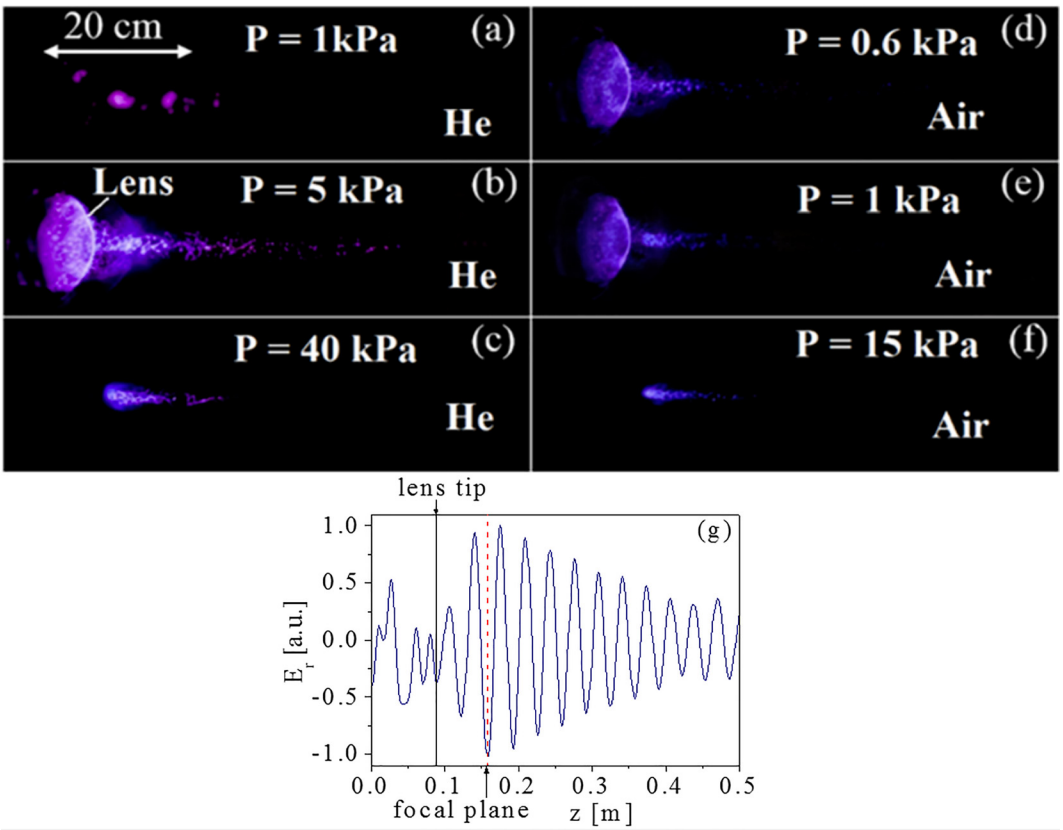

FIG. 10. Time-integrated side view of the light emission from the microwave-generated plasma for He: (a) 10^3 Pa, (b) 5×10^3 Pa, (c) 4×10^4 Pa; and air: (d) 6×10^2 Pa, (e) 10^3 Pa, and (f) 1.5×10^4 Pa. (h) Time integrated view of the radial component of the electric field on axis of the Pyrex tube obtained by MAGIC simulations in vacuum (g).

IV. DISCUSSION

The experimental results described in Sec. III show that, depending on the neutral gas pressure p, three different regimes of the microwave beam's propagation and plasma formation can be distinguished. At low pressure, $P < 1.5 \times 10^3$ Pa for He and $p < 5 \times 10^2$ Pa for air, the beam propagation is not affected by the produced plasma. The plasma appears first near the focal plane and forms a diffused spatial structure, while its density remains small compared to the critical density during the crossing time of the pulse and it does not increase further. At high pressure, $p > 8 \times 10^4$ Pa for He and $p > 1.5 \times 10^4$ Pa for air, the behavior is similar apart from the observed streamer-like structures. This difference is the natural consequence of the dependence of the electron's mean free path on gas pressure. These peculiarities of sub-nanosecond time scale plasma formation were observed experimentally and analyzed in the earlier research.[9,15–25]

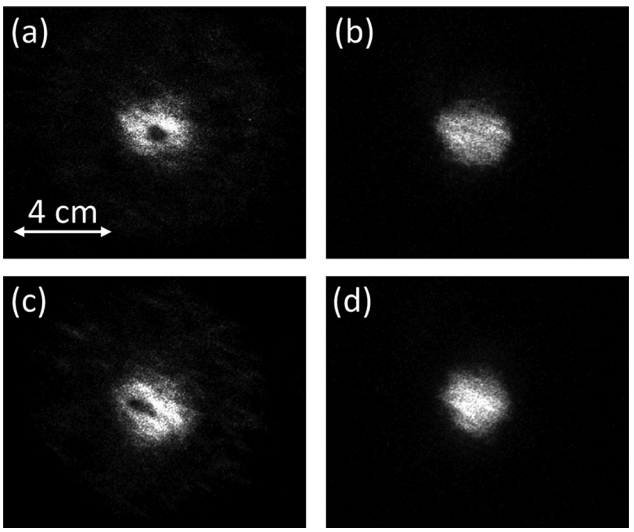

FIG. 11. Front view fast framing images of the plasma obtained for air (a)10^3 Pa; (b)1.5×10^4 Pa, and for He (c)4.5×10^3 Pa; (d)3×10^4 Pa. The frame duration is of 1.2 ns.

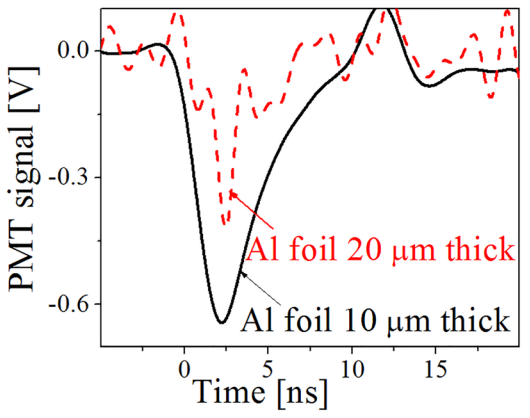

FIG. 12. The luminescence signal from the fast plastic scintillator covered by a 10 μm thick Al foil (solid back line) and by a 20 μm (dashed red line), positioned at $r = 4.5$ cm from the axis of the Pyrex tube at the focal plane, for air at $p = 1.5 \times 10^3$ Pa.

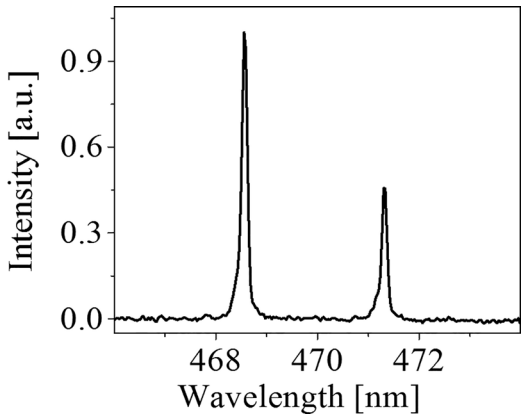

FIG. 13. Typical line spectrum, showing the lines of He I (471.3 nm) and He II (468.7 nm), obtained for He at $p = 4.5 \times 10^3$ Pa. Here the frame duration of the 4QuikE camera is 10 ns.

At intermediate pressures, the beam propagation and the plasma formation strongly differ from that described above. Features peculiar to this region are the following: (i) the microwave power that reaches the receiving antenna decreases by factors of ~2–3; (ii) the waveform of the microwave pulse which reaches the receiving antenna differs from the incoming one; (iii) the appearance of the hollow plasma structure near the focal plane, for wave amplitudes ≥ 150 kV/cm; (iv) only central light emission pattern obtained by the Ne lamp array; and (v) formation of long, many Rayleigh lengths, plasma "tail" beyond the focus. All these features can be consistently explained by ionization-induced self-guiding of powerful microwave pulses, as follows.

Depending on the microwave beam and gas parameters, various phenomena can be responsible for a guiding channel formation. One of these is the ponderomotive force caused by the radial gradient of the oscillating electric field, which pushes the electrons outward from the beam's axis.[40] Enhanced plasma density at the beam periphery reflects the electromagnetic waves preventing the beam's divergence. Another phenomenon occurs when the wave amplitude is so large that the relativistic increase in the mass of the oscillating electrons becomes important. Then, the effective plasma frequency becomes higher at the beam periphery which again leads to suppression of the beam's divergence.[41] Plasma heating and radial expansion can also lead to the formation of a plasma guiding channel,[42] but this mechanism is important only for long beam pulses.

Simple estimates show that for 9.6 GHz oscillating electric fields with amplitude $\leq$150 kV/cm, none of the above phenomena can explain the present experimental data. For the above-mentioned phenomena, it is important to note that the guiding profile of the plasma density appears as a result of the nonlinear interaction of the plasma with the beam, while the ionization process itself is only of secondary importance. There are, though, conditions for which the non-monotonic dependence of the impact ionization cross section σ_i on the electron energy can become a sufficient reason for the formation of a plasma channel in which the electromagnetic beam is guided.[30] This can occur when the electron energy is large enough, larger on axis, and decreases radially, and the value of σ_i is a decreasing function of the energy. This will cause the ionization rate to be smaller on the beam axis than at its periphery resulting in plasma formation with a focusing radial profile.

TABLE I. The measured excited He I level population calculated by collisional radiative modeling. Data obtained for He at $P = 4.5 \times 10^3$ Pa.

Energy level	Population (10^{11} Excited atoms/cm^3)
He I, 1s3d(^{3}D)	7.9±0.7
He I, 1s3d (^{1}D)	80±5
He I, 1s3p(^{3}P)	27±2
He I, 1s4s (^{1}D)	4.6±0.3
He I, 1s4d (^{1}D)	22±1.5
He II, $n = 4$	0.07±0.01

Let us consider a model of the plasma formation due to neutral gas ionization by a powerful microwave beam. The time evolution of the electron density, n_e, is described by

$$n_e(t) = n_0 e^{n_g \int_{-\infty}^{t} dt' \sigma(w)|\mathrm{v}|}, \quad (1)$$

where n_g is the neutral gas density and n_0 is an initial uniform background electron density, v and w are the electron velocity and kinetic energy, respectively, and σ is the electron impact ionization cross-section. The amplitude of the electron spatial oscillations in an electric field of the strength $E_0 = 150$ kV/cm and frequency $f = 10$ GHz is $\tilde{a} = eE_0/m\omega^2 \approx 0.07$ cm. This is significantly smaller than the microwave beam diameter at the focal plane, so that the ionization process can be considered as a local function of the radius. As it will become clear below, it is convenient to use the quantity $\mathcal{E} = 10^{-5}E\,[\mathrm{V/cm}]$ as a scaled value of the electric field. Then, $w[\mathrm{eV}] = (10^4/4\pi^2)(\mathcal{E}\lambda)^2\cos^2(\omega t)$ and $\mathrm{v} = (0.1c/\pi)(\mathcal{E}\lambda)\cos(\omega t)$, where λ is the microwave wavelength in cm and ω is the microwave angular frequency. For a Gaussian microwave beam of maximum amplitude ε_{00}, the electric field amplitude's dependence on r and t is given as

$$\mathcal{E}(r,t) = \mathcal{E}_0(r)e^{-t^2/2\tau_{beam}^2}, \quad \mathcal{E}_0(r) = \mathcal{E}_{00}e^{-r^2/2r_{beam}^2}, \quad (2)$$

where r_{beam} and τ_{beam} are the radial and temporal Gaussian widths of the beam. If $\omega\tau_{beam} \gg 1$, it is convenient to use quantities averaged over the period of the field oscillation and present the integral $\int_{-\infty}^{t} dt'\sigma(w)|v|$ in Eq. (1) as follows:

$$\int_{-\infty}^{t} dt'\sigma|\mathrm{v}| = \frac{0.1c}{\pi}\tau_{beam}\int_{-\infty}^{\theta=t/\tau_{beam}} d\theta' e^{-\theta'^2/2} I_1\left[\mathcal{E}_0(r)\lambda;\theta'\right] \equiv \frac{0.1c}{\pi}\tau_{beam}F(\theta;a). \quad (3)$$

Here $\theta = t/\tau_{beam}$, $a = \mathcal{E}_0(r)\lambda$, and the function I_1 is defined as

$$I_1\left[\mathcal{E}_0(r)\lambda;\theta'\right] = \frac{1}{2\pi}\left[\mathcal{E}_0(r)\lambda\right]\int_{-\pi}^{\pi} d\tau|\cos\tau| \times \sigma\left\{\frac{10^4}{4\pi^2}\left[\mathcal{E}_0(r)\lambda\right]^2 e^{-\theta'^2}\cos^2\tau\right\}, \quad (4)$$

where $\tau = \omega t$ and the value of σ is measured in units of 10^{-16} cm^2.[39] The dependence of $F(\theta; a)$ on θ for various values of the parameter a is shown in Fig. 14 for He.

The function $F(\theta; a)$ is a monotonically increasing function of a for any time t until $a < 4$ (compare curves for $a = 0.5, 1.0, 2.0, 4.0$ in Fig. 14). This means that for $a < 4$, the plasma density $n_e(t, r)$ is maximal on the beam axis, where the electric field is maximal, and decreases from the axis towards the beam periphery. A different behavior is observed when the parameter a, i.e., electric field, is large enough, $a > 4$. During the first half of the pulse, the larger the electric field, the larger is the function $F(\theta, a)$. In contrast, during the second half of the pulse, the function $F(\theta, a)$ decreases as the field amplitude grows (compare dependencies for $a = 4$ and $a = 9$ in Fig. 14). It means that the plasma density is maximal on the beam axis during the first half of the pulse duration, and it becomes smaller on axis than at larger radii during the second half of the pulse. The plasma density reaches its maximal value at a certain radius $r > 0$, forming the observed plasma channel. The threshold value of the electric field, i.e., $a \geq 4$, $E \geq 130$ kV/cm, for this phenomenon to occur, and it is almost the same for He and air. Above this threshold value, the plasma density, after the beam propagation ($\theta \approx 2$,) is practically independent of the electric field, resulting in the value $F(\theta, a) \approx 0.8$. The latter allows one to estimate the plasma density after the pulse propagation as

$$\ln(n_{final}/n_0) \approx 10^{-16} A p \tau_{beam}. \quad (5)$$

Here p is the pressure in Torr, τ_{beam} is the beam duration in ns, and A is a coefficient equal to 2.8 and 20 for He and air, respectively, due to the difference in ionization cross-sections for these gases. An example of the plasma density evolution in time and space for He and a field amplitude of $a = 5$ ($E \approx 170$ kV/cm) is shown in Fig. 15.

One can see that the plasma density has a maximal density at radius $r \approx r_{beam}$ at the normalized time $\theta \approx 1.2$. The beam can propagate through this guiding profile of the plasma density (plasma channel) if the density on axis is smaller than critical, n_c: $n_e|_{t \approx \tau_{beam}} < n_c \approx 1.23 \cdot 10^{12}$ cm^{-3} for 10 GHz microwaves. Using the experimental value of the electric field amplitude $E \approx 150$ kV/cm, and assuming, that $n_0 \approx 10^5$ cm^{-3},

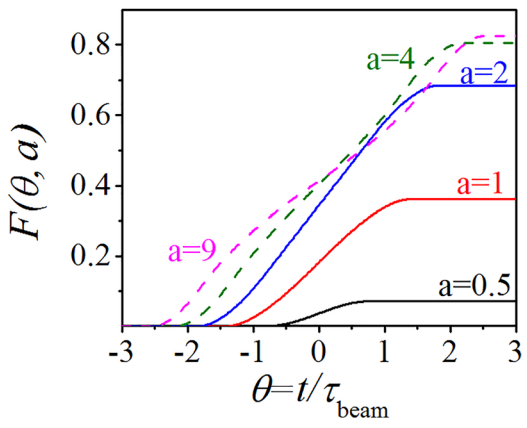

FIG. 14. The dependence of the function $F(\theta; a)$ on θ for different values of a in He. Here $\theta = 0$ corresponds to the temporal center of the pulse.

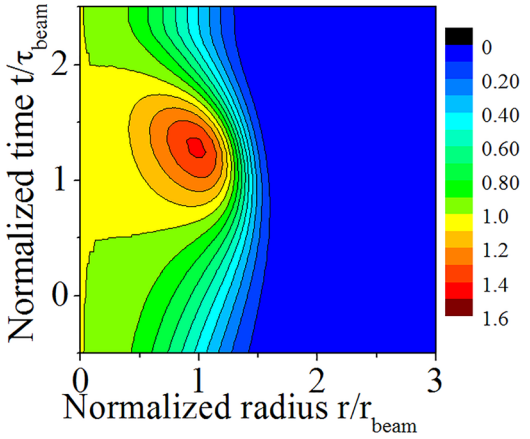

FIG. 15. Contour plot of the plasma density (in He) versus the microwave beam normalized radius and time, $a = \mathcal{E}_{00}\lambda = 5$. The density is normalized by its value $n(t, 0)$ on the beam's axis.

one can calculate that at $\tau \approx \tau_{beam} \approx 0.37$ ns self-channeling occurs at $p \approx 4 \times 10^3$ Pa for He and $p \approx 6 \times 10^2$ Pa for air. These values are close to the pressures for which this effect is observed experimentally. For air and helium at pressures smaller than 10^3 Pa and 4×10^3 Pa, respectively, the plasma is collisionless, i.e., $\nu \ll \omega$. The skin layer δ_c at the beam's periphery, where the plasma density exceeds the critical value necessary for microwave cut-off, can be estimated as $\delta_c = c/\omega_{pe} \approx 0.7$ cm, which is significantly smaller than the beam diameter.

Estimation of the final plasma density n_{final} shows a density buildup $\geq 10^{14}$ cm^{-3}, which coincides well with the spectroscopic data. The assumed density of the initial background electrons is not exaggerated because prior to the beam's arrival to the interaction chamber, a ~5 ns x-ray flux is generated by the electron beam collected on the conducting walls at the output of the BWO and a ~2 ns microwave pre-pulse with an electric field amplitude of ~15 kV/cm is also present.

To support our model, a numerical study of the plasma formation was carried out using a one-dimensional (1D) PIC Monte Carlo collisional simulation code (a detailed description of this code is presented in Ref. 32). The code accounts for the electron-neutral momentum transfer collisions, excitation of electronic levels of neutrals, and ionization processes. In these simulations, a one-dimensional oscillating electric field was introduced with a peak amplitude E = 150 kV/cm $\tau_{beam} = 0.37$ ns and $r_{beam} = 1.6$ cm. The plasma was generated by the electron impact ionization of air or He started by a seed electron density of 10^5 cm^{-3}. An example of the plasma density and the electron energy distribution function (EEDF), for He at $p = 4.5 \times 10^3$ Pa, is shown in Fig. 16. The results of these simulations show that at the peak of the pulse in He at $p = 4.5 \times 10^3$ Pa, the plasma density reaches $n_e \approx 2.3 \times 10^{12}$ cm^{-3} and $n_e \approx 6 \times 10^{11}$ cm^{-3}, at $r = 2$ cm and $r = 0$, respectively. Such a density profile allows only the central part of the microwave beam to transit through the plasma with reflection from the over-dense plasma "walls," formed at the beam periphery. Similar results were obtained for air at 10^3 Pa. For higher gas pressures, the plasma density grows above the critical level too early, so that the microwave beam is reflected backward before a guiding structure

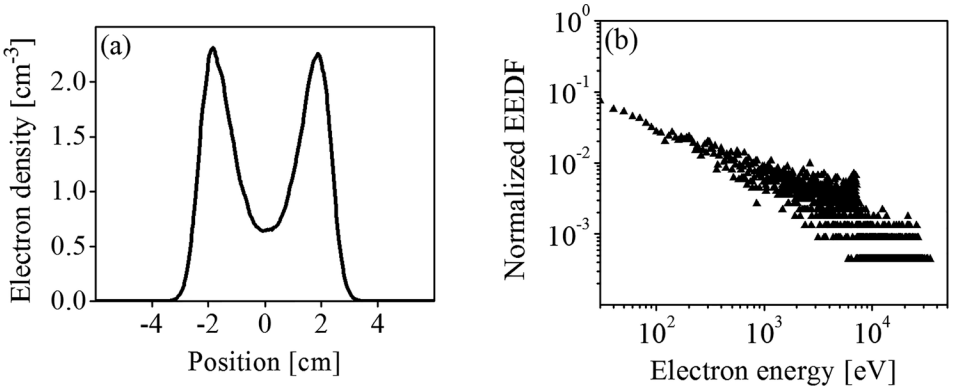

FIG. 16. The normalized electron density vs. the radial position (a) and the normalized EEDF (b), simulated by the 1D-PIC Monte Carlo code.[23] The presented data are for He at $p = 4.5 \times 10^3$ Pa, at the peak of the pulse.

can form. When the amplitude of the electric field is less than 150 kV/cm, no channeling develops. These simulations also show that the plasma electrons acquire energies up to ~40 keV and that most electrons have energies ≥ 100 eV [see Fig. 16(b)]. These energetic electrons, with an ionization mean free path $\lambda_i \approx (n_g \sigma_{ion})^{-1} \approx 0.25$ cm, continue ionizing the neutral gas resulting in the increase of the plasma density long after the microwave beam has left the focal plane. For both air and He, the plasma density exceeds 10^{14} cm^{-3} at $t \approx 2$ ns. These results agree well with the experimental measurements of the high energy electrons ($\geq$15 keV) and with the results of our spectroscopic study of the plasma electron density ($t \geq 2$ ns).

The analytical model and the 1D calculations presented above do not account for the propagation of the microwave beam through a non-stationary non-uniform plasma. Nevertheless, both sets of results reproduce the important peculiarities of the observed phenomena. Moreover, the calculated threshold value of ~150 kV/cm agrees with the experiment. Second, only the central part of the pulse, where $E > E_{cr}$, produces the enhanced value of the plasma density at the beam periphery (the duration of the central part depends on the maximum amplitude). During the time intervals before and after this central part, where $E < E_{cr}$, the plasma is produced mainly near the beam axis, which decreases the efficiency of the beam's guiding. Lastly, to create a long plasma channel, it is desirable that the time required for the plasma density's growth to the critical value, t_{ion}, will be approximately the same as the wave propagation time along the channel of length l_{chan} and the pulse duration: $t_{ion} \simeq \tau_{beam} \simeq l_{chan}/c$. Equation (5) connects the pulse duration with the gas pressure. Thus, to create a long channel, it is necessary to increase the pulse duration and simultaneously decrease the gas pressure. The parameters of the microwave source (maximum amplitude in the focal plane and pulse duration) in our experiments do not fulfill all these requirements simultaneously resulting in a relatively short plasma channel and a life time of less than 1 ns.

In order to demonstrate how efficient ionization-induced channeling can be, two-dimensional (2D) hybrid PIC simulations were performed using the large-scale plasma (Lsp) PIC software package. In these simulations, a Gaussian microwave (10 GHz) beam with a rectangular leading front is injected into the interaction space. The beam is characterized by a focal spot-size Gaussian radius of 2.3 cm at a focal plane at $z = 18$ cm. The wave propagates along the $[z, x]$ area which is taken large enough to minimize boundary reflections. This space is filled uniformly with He, $n_g = 1.64 \times 10^{17}$ cm^{-3}, and uniformly distributed background electrons, $n_0 = 10^6$ cm^{-3}. In these simulations, electron impact ionization and four of the most important excitation reactions are accounted for, using cross section function given by Ralchenko *et al.*[39] and energy loss by Monte Carlo scattering. Only electron dynamics is considered, whereas atoms and ions are stationary. When appropriate, Lsp becomes *hybrid*; that is, kinetic electrons can migrate to become fluid particles with fluid dynamics governing their motion. The latter prevents artificial plasma electron heating because of finite Debye radius in PIC simulations.

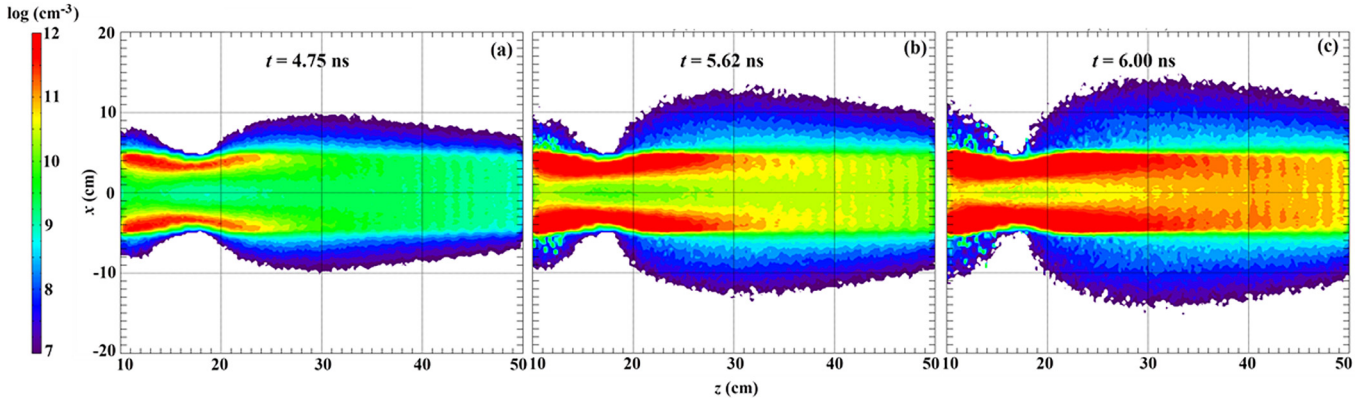

FIG. 17. Time- and space-resolved evolution of the density of the plasma generated by microwave beam ionization of He during beam propagation obtained by Lsp simulations.

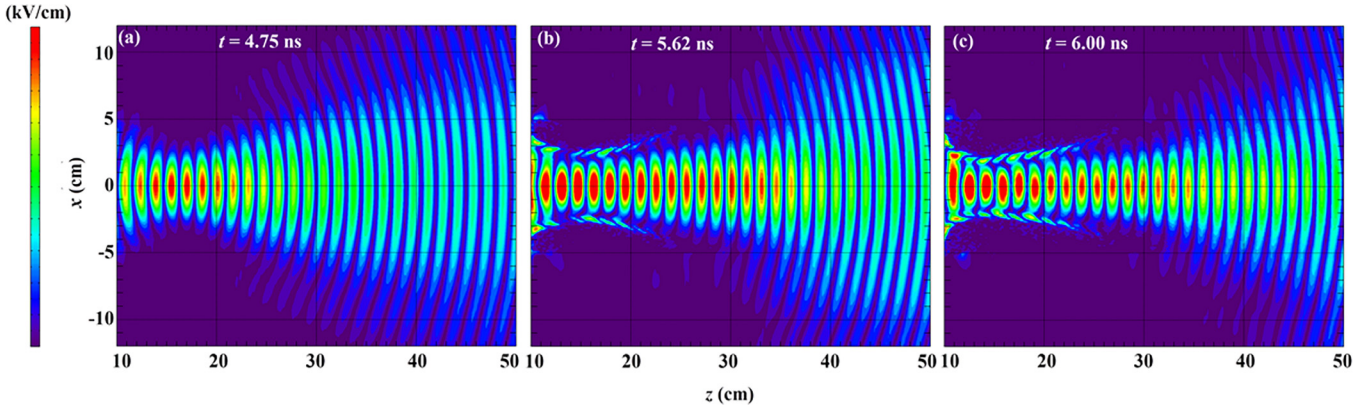

FIG. 18. Time- and space-resolved evolution of the electric field $|E_x|$ of the propagating microwave beam obtained by Lsp simulations. The electric field ranges in (a) between 0 and 200 kV/cm, whereas in (b) and (c) 0–150 kV/cm and the contour colors scale accordingly.

The observed ionization time t_{ion} is rather long; namely, it takes ~4.5 ns to reach critical plasma density ($\sim 10^{12}$ cm^{-3}) at the periphery of the beam [Fig. 17(a)]. In time [Figs. 17(b) and 17(c)], the plasma channel develops and fills in. In Fig. 18, contours of $|E_x|$ at the same times as the corresponding panels of Fig. 17 are drawn. In Fig. 19, one can see that the plasma electrons can reach keV range energies as a result of acceleration by the microwave beam electric fields in agreement with the experimental results.

The critical plasma density walls seen in Fig. 17 develop into a conical, almost closed plasma formation, much longer than the Rayleigh length, as seen in the experiment [see Fig. 10(b)]. The open channel seen here closes in ~1.5 ns. Thus, only during 1–2 ns, one can expect channeling and self-focusing to occur. In Fig. 20, the time dependence of the absolute value of the electric field (red) on axis at $z = 30$ cm, i.e., 12 cm downstream from the focal point, is presented.

The horizontal red line in Fig. 20 represents the amplitude level of the same electric field when the beam propagates in vacuum. Thus, the peaks above the vacuum line represent fields reflected from the channel walls. After these peaks, the electric field drops due to plasma density cutoff. In the simulations with higher gas pressure, the channel closes much faster and cutoff appears before self-focusing, as it follows from the analysis presented above.

The experimental results described in Sec. III agree qualitatively with the results of the analytical model and the numerical simulations. The microwave beam pattern obtained by the array of Ne lamps shows a significant decrease in the beam diameter for $p = 4.5 \times 10^3$ Pa for He and $p = 7 \times 10^2$ Pa for air in contrast to pressures below or above. For these values within the intermediate pressure regions, the appearance of two peaks in the transmitted signal, separated by a time interval of about 0.5 ns, is typical (see Fig. 4). Also, as one can see in Fig. 21, the frequency of the transmitted second peak is slightly upshifted in frequency.

The possible qualitative explanations of these two peaks in the transmitted signal are the following. At the beginning of the pulse, when the wave amplitude is small, the plasma is generated mainly near the focal plane around the beam axis, as shown in Fig. 15. This profile of the plasma density enhances the radial divergence of the microwave beam, which, together with the microwave energy dissipation, results in the decrease in the receiving antenna signal. Closer to the pulse maximum, when the wave amplitude is large, plasma is produced much faster at the beam periphery than on the axis, forming the channel with "walls" of denser (even over-critical) plasma, so that part of the diverged waves become captured in the channel and reach the antenna as a second maximum.

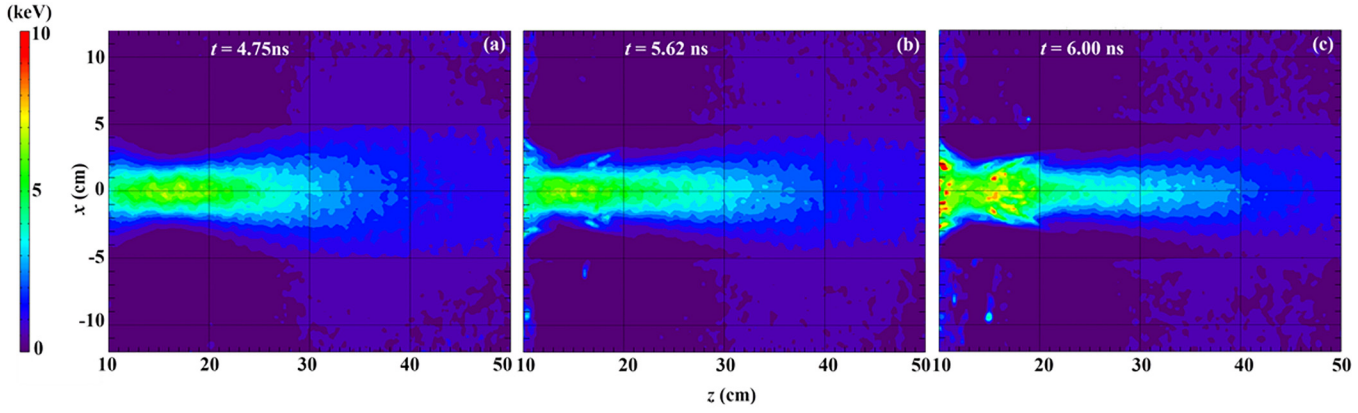

FIG. 19. Time- and space-resolved evolution of the plasma electron energy during the propagation of the microwave beam.

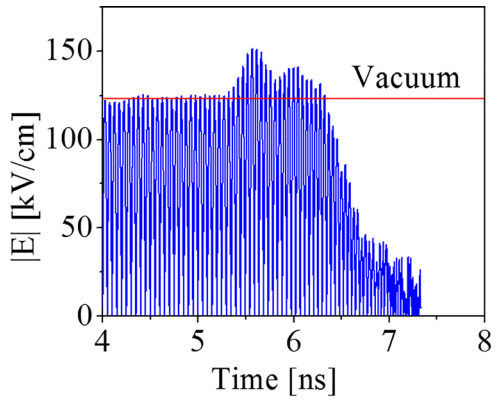

FIG. 20. Time dependence of the electric field on axis at $z = 30$ cm.

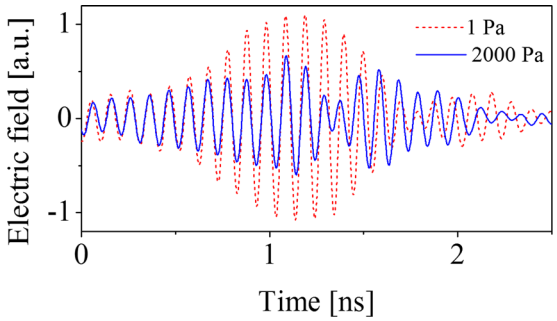

FIG. 21. Typical temporal dependence of electric field of the transmitted signal, measured at the receiver antenna in vacuum (a) and intermediate (b) air pressure.

V. CONCLUSION

In this paper, the interaction of a high power ($\leq$500 MW), sub-ns microwave beam with neutral gas was studied using microwave, optical, and electrical methods. For the first time, impact ionization-induced self-channeling of a high-power, short duration focused microwave beam, injected into a gas, was observed. The guiding of the beam along a few Rayleigh lengths occurs due to the larger oscillating electron energy and, consequently, slower ionization rate on the beam axis than at its periphery. There is qualitative agreement between the experimental observations and the results of an analytic model, describing the evolution of the plasma density at the focal plane, and with PIC simulations.

ACKNOWLEDGMENTS

The authors are grateful to E. Schamiloglu, Y. Slutsker, and Y. Hadas for fruitful discussions, to E. Flyat, J. Gleizer, and S. Gleizer for their technical assistance. This work was supported in part by the PAZY Grant No. #2020960 and research program of the RAS #10.

[1]J. Benford, J. Swegle, and E. Schamiluglu, *High Power Microwaves*, 2nd ed. (CRC Press, 2001).
[2]H. Ito, Y. Nishida, and N. Yugami, Phys. Rev. Lett. **76**, 4540 (1996).
[3]H. Ito, C. Rajyaguru, N. Yugami, Y. Nishida, and T. Hosoya, Phys. Rev. E **69**, 066406 (2004).
[4]G. Shafir, A. Shlapakovski, M. Siman-Tov, Y. Bliokh, J. G. Leopold, S. Gleizer, R. Gad, V. V. Rostov, and Y. E. Krasik, J. Appl. Phys. **121**, 33301 (2017).
[5]Y. P. Bliokh, J. G. Leopold, G. Shafir, A. Shlapakovski, and Y. E. Krasik, Phys. Plasmas **24**, 63112 (2017).
[6]H. K. Malik and S. Kumar, Laser Part. Beams **26**, 197 (2008).
[7]A. K. Aria and H. K. Malik, Open Plasma Phys. J. **1**, 1 (2008).
[8]A. K. Aria and H. K. Malik, Opt. Commun. **282**, 423 (2009).
[9]A. L. Vikharev, O. A. Ivanov, and A. G. Litvak, IEEE Trans. Plasma Sci. **24**, 460 (1996).
[10]L. Beilin, A. Shlapakovski, M. Donskoy, T. Queller, and Y. E. Krasik, EPL (Europhys. Lett.) **109**, 25001 (2015).
[11]A. S. Shlapakovski, L. Beilin, Y. Hadas, E. Schamiloglu, and Y. E. Krasik, Phys. Plasmas **22**, 73111 (2015).
[12]R. M. Gilgenbach, M. E. Read, K. E. Hackett, R. Lucey, B. Hui, V. L. Granatstein, K. R. Chu, A. C. England, C. M. Loring, O. C. Eldridge, H. C. Howe, A. G. Kulchar, E. Lazarus, M. Murakami, and J. B. Wilgen, Phys. Rev. Lett. **44**, 647 (1980).
[13]V. B. Gil'denburg, A. G. Litvak, and N. A. Zharova, Phys. Rev. Lett. **78**, 2968 (1997).
[14]P. Felsenthal, J. Appl. Phys. **37**, 4557 (1966).
[15]M. Brizhinev and A. Vikharev, Sov. Phys. JETP **71**, 242 (1990).
[16]A. Vikharev, in *Proceedings of International Workshop on "Strong Microwaves Plasmas"* (1991), pp. 306–323.
[17]A. L. Vikharev, J. Phys. IV France **8**, Pr7-275 (1998).
[18]A. L. Vikharev, V. B. Gil'denburg, S. V. Golubev, G. Eremin, A. Ivanov, A. G. Litvak, A. N. Stepanov, and A. D. Yunakovskii, Sov. Phys. JETP **67**(4), 724 (1988).
[19]A. Cook, M. Shapiro, and R. Temkin, Appl. Phys. Lett. **97**, 011504 (2010).
[20]Y. Hidaka, E. M. Choi, I. Mastovsky, M. A. Shapiro, J. R. Sirigiri, and R. J. Temkin, Phys. Rev. Lett. **100**(3), 035003 (2008).
[21]Y. Hidaka, E. M. Choi, I. Mastovsky, M. A. Shapiro, J. R. Sirigiri, R. J. Temkin, G. F. Edmiston, A. A. Neuber, and Y. Oda, Phys. Plasmas **16**, 055702 (2009).
[22]G. M. Batanov, V. A. Ivanov, M. E. Konyzhev, A. A. Ravaev, V. D. Selesnev, and A. I. Khomenko, in *Proceedings of International Workshop on "Strong Microwaves Plasmas"* (1991), p. 553.
[23]S. V. Bulanov, L. M. Kovrizhnykh, and A. S. Sakharov, Phys. Rep. **186**, 1 (1990).
[24]M. I. Yalandin, V. G. Shpak, S. A. Shunailov, M. R. Oulmaskoulov, N. S. Ginzburg, I. V. Zotova, Y. V. Novozhilova, A. S. Sergeev, A. D. R. Phelps, A. W. Cross, S. M. Wiggins, and K. Ronald, IEEE Trans. Plasma Sci. **28**, 1615 (2000).
[25]M. I. Yalandin, A. G. Reutova, K. A. Sharypov, V. G. Shpak, S. A. Shunailov, M. R. Ul'masculov, and G. A. Mesyats, IEEE Trans. Plasma Sci. **38**, 1398 (2010).
[26]S. C. Wilks, J. M. Dawson, and W. B. Mori, Phys. Rev. Lett. **61**, 337 (1988).
[27]X. Xu, N. Yugami, and Y. Nishida, Phys. Rev. E **55**, 3328 (1997).
[28]V. B. Gildenburg, V. A. Krupnov, and V. E. Semenov, Sov. Tech. Phys. Lett. **14**, 738 (1988).
[29]S. P. Kuo, Phys. Rev. Lett. **65**, 1000 (1990).
[30]Y. L. Bogomolov, S. F. Lirin, V. E. Semenov, and A. M. Sergeev, JETP Lett. **45**, 680 (1987).
[31]D. Levko, S. Yatom, V. Vekselman, J. Z. Gleizer, V. T. Gurovich, and Y. E. Krasik, J. Appl. Phys. **111**, 013304 (2012).
[32]D. R. Welch, D. V. Rose, B. V. Oliver, and R. E. Clark, Nucl. Instrum. Methods Phys. Res., Sect. A **464**, 134 (2001).
[33]D. R. Welch, D. V. Rose, M. E. Cuneo, R. B. Campbell, and T. A. Mehlhorn, Phys. Plasmas **13**, 063105 (2006).
[34]A. A. Eltchaninov, S. D. Korovin, G. A. Mesyats, I. V. Pegel, V. V. Rostov, V. G. Shpak, and M. I. Yalandin, IEEE Trans. Plasma Sci. **32**, 1093 (2004).
[35]S. N. Rukin, Instrum. Exp. Tech. **4**, 439 (1999).
[36]Y. V. Ralchenko and Y. Maron, J. Quant. Spectrosc. Radiat. Transf. **71**, 609 (2001).
[37]B. Goplen, L. Ludeking, D. Smith, and D. Warren, Comput. Phys. Commun. **87**, 54 (1995).
[38]M. J. Berger, J. S. Coursey, M. A. Zucker, and J. Chang, see http://www.nist.gov/pml/data/star/index.cfm for NIST (2011).
[39]Y. Ralchenko, R. K. Janev, T. Kato, D. V. Fursa, I. Bray, and F. J. de Heer, At. Data Nucl. Data Tables **94**, 603 (2008).
[40]G.-Z. Sun, E. Ott, Y. C. Lee, and P. Guzdar, Phys. Fluids **30**, 526 (1987).
[41]P. Sprangle, C. M. Tang, and E. Esarey, IEEE Trans. Plasma Sci. **15**, 145 (1987).
[42]F. W. Perkins and E. J. Valeo, Phys. Rev. Lett. **32**, 1234 (1974).